Correlation of Spatiotemporal Dynamics of Polarization and Charge Transport in Blended Hybrid Organic–Inorganic Perovskites on Macro- and Nanoscales

Liam Collins,* Eric S. Muckley, Hsinhan Tsai, Dibyajyoti Ghosh, Amanda J. Neukirch, Sergei Tretiak, Sergei V. Kalinin, Wanyi Nie, and Ilia N. Ivanov*

Cite This: *ACS Appl. Mater. Interfaces* 2020, 12, 15380−15388

Read Online

ACCESS | Metrics & More | Article Recommendations | SI Supporting Information

ABSTRACT: Progress in flexible organic electronics necessitates a full understanding of how local inhomogeneities impact electronic and ionic conduction pathways and underlie macroscopic device characteristics. We used frequency- and time-resolved macro- and nanoprobe measurements to study spatiotemporal characteristics of multiscale charge transport dynamics in a series of ternary-blended hybrid organic inorganic perovskites (HOIPs) ($MA_{0.95−x}FA_xCs_{0.05}PbI_3$). We show that A-site cation composition defines charge transport mechanisms across broad temporal (10^2–10^{-6} s) and spatial (millimeters–picometers) scales. Ab initio molecular dynamic simulations suggest that insertion of FA results in a dynamic lattice, improved ion transport, and dipole screening. We demonstrate that correlations between macro- and nanoscale measurements provide a pathway for accessing distribution of relaxation in nanoscale polarization and charge transport dynamics of ionically conductive functional perovskites.
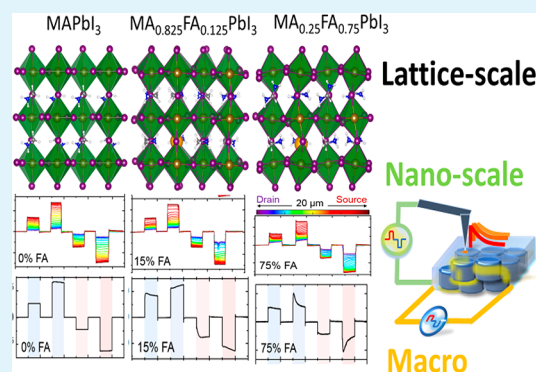
INTRODUCTION

Hybrid organic—inorganic perovskites (HOIP) hold promise for next-generation optoelectronic applications in part due to favorable energy conversion efficiencies, lossless carrier transport, low-cost solution processing, and tunable bandgap.[1−3] Despite a relatively simple chemical structure, HOIPs have been shown to be inherently complex materials which support a diverse range of dynamic physical and chemical processes central to optoelectronic applications. Unusual device characteristics reported in HOIP, including giant low-frequency dielectric response,[4] current—voltage hysteresis,[5−13] and slow transient behavior,[12] often impact power conversion efficiency[10,14] and stability.[15−17] Dynamic hysteresis is linked to solar cell degradation[8,18] and commercial feasibility of HOIP. Anomalous device behavior is often mitigated by facile chemical synthesis, modification of device architectures, or standardization of measurement protocols.[10,14,19]

Dynamic hysteresis (normal, inverted, or mixed) in HOIP devices (commonly observed for different scan rates and poling voltage bias) were linked to changes in interfacial charge trapping[13] and dipole screening,[20,21] electrochemical doping of the interfacial region,[22,23] ferroelectric polarization, and migration of mobile ions/vacancies.[8] It was shown that hysteresis can be suppressed by tuning the properties of interface materials.[25,7,9,23] Normal hysteresis can be switched to inverted hysteresis by application of negative prepoling bias or to mixed hysteresis for intermediate conditions. Ion migration was observed even in devices with minimal hysteresis,[7] while the dynamic electrical model describes time-dependent polarization charge moving toward equilibrium states.[10]

A broad range of experimental parameters (e.g., bias scan rate, range, direction, stabilized open circuit voltage, and poling voltage) affecting hysteresis have been identified which suggest that slow dynamics are associated with ion migration. However, further investigation is needed to clarify the nature of ionic species, effects of organic cations on hysteresis and transport, and slow transient behaviors in mixed HOIP.

It is difficult to simultaneously probe organic and inorganic ion diffusion,[24] rotation,[25−27] octahedral distortions,[27,28] and time and length scales of charge and ion diffusion. A
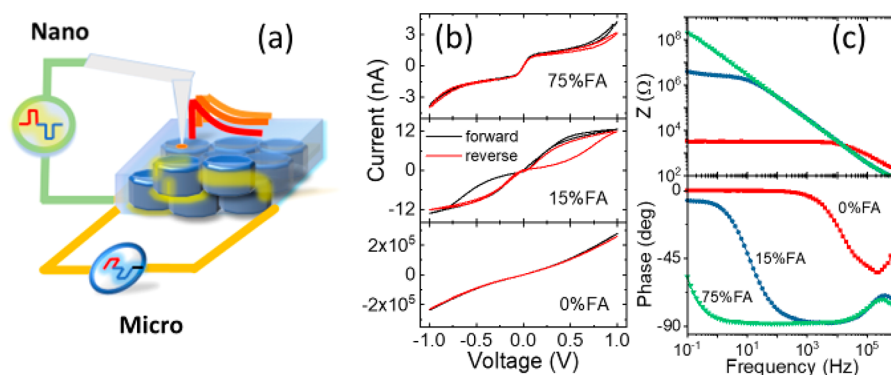
Figure 1. (a) Schematic principle of the multiscale characterization of HOIP. (b) Linear voltammetry measured in forward (black) and reverse (red) directions from 0 V → ±1 V → ±1 V → 0 V with a sweep rate of 20 mV/s. (c) Bode plots of impedance (top panel) and phase (bottom panel) measured from 0.1 Hz to 1 MHz for 15% and 75% FA.

combination of molecular dynamic simulations with scanning transmission electron microscopy, electron energy loss spectroscopy, and advanced KPFM modes was applied for detection of mobile and immobile species and their correlation with enhanced or suppressed hysteretic behavior in perovskite photovoltaics.[29]

Small-amplitude perturbation frequency-dependent impedance spectroscopy (IS), which allows probing of charge and ion transport in hybrid perovskite solar cells, revealed the importance of transport resistance of TiO_2 layers,[5] ionic transport in perovskite quantum dots solar cells,[30] conditions for $J-V$ response stabilization,[31] and hysteresis behavior of solar cells upon replacement of methylammonium with formamidinium and cesiumium.[32] However, most published research on hybrid perovskites were performed on complete photovoltaic cells, where multiple interface effects influenced processes in the perovskite layer.[32,33] There has been little attempt to correlate observed dynamics of frequency- and time-dependent response on macro- and nanoscales using pure HOIP film or correlation of changes in relaxation time without extraction of ambiguous fitting parameters from IS spectra.[34]

Here we demonstrate the possibility of correlating experimentally measured nanoscale charge transport dynamics and macroscopic behavior to decipher the role of A-site cations on hysteresis in a series of ternary blended HOIP devices ($MA_{0.95-x}FA_xPbI_3$) across broad length (nanometers−micrometers) and time (microseconds−seconds) scales. We demonstrate a suite of complementary experimental techniques and modeling which allows probing of correlations in charge/ion transport dynamics in time and frequency domains on macro- and nanoscales as well as visualization of spatial and temporal distribution of relaxation processes in perovskite film and at the electrode interface as a function of $MA_xFA_{1-x}PbI_3$ film composition. Using *ab initio* molecular dynamic (AIMD) simulations, we further correlate macroscale and nanoscale measurements with atomic scale structural fluctuations. Our results indicate that insertion of larger FA cations in the organic framework leads to a more "dynamic" lattice favoring reorientation of the cation dipole as well as a lowering of the activation potential for migration of ionic species with increasing FA.

■ RESULTS AND DISCUSSION

Multiscale Characterization. After the application of a voltage to a HOIP, fast ($\sim 10^{-3}-10^{-9}$ s) orientational and dipolar polarization processes can arise due to the alignment of

intrinsic permanent dipoles parallel to the electric applied field. At longer time scales ($10^{-3}-10^2$ s), space charge polarization involving accumulation of charges at interfaces dominates motion of ionic and covalent bonded structures as well as mobile charges on the nanometer to micrometer length scale.[22]

The multiscale nature of these dynamic processes necessitates characterization of charge/ion transport mechanisms in HOIP with multiscale spatial and temporal resolution. The generalized approach shown schematically in Figure 1a combines experimental probes which cover multiscale spatial and temporal ranges to describe the charge transport in HOIP.

We correlate response from micrometer scale frequency- and time-dependent techniques with local (nanoscale) dynamics captured by time-resolved Kelvin probe force microscopy (tr-KPFM),[35,36] complementing insights into the atomic energetic landscapes obtained from AIMD simulations. To avoid sample degradation, characterization of macro and local properties was performed on the same HOIP under the controlled environment. We employed an in-plane sample configuration where all samples were grown directly on SiO_2/Si substrates with prepatterned interdigitated platinum electrodes with 20 μm separation. This design enabled probing of the active HOIP layer without undesirable effects from the charge transport layers.

In mixed HOIP films, little is known about the precise role of the cation composition on polarization and screening mechanisms. At the same time ternary mixed cations are of interest as they have been shown to improve stability in these materials. To check the influence of the A-site cation on macroscale hysteresis, a series of $MA_{0.95-x}FA_xPbI_3$ films ($x = 0\%$, $x = 15\%$, $x = 75\%$) were tested by current−voltage (JV) measurements in forward and reverse directions, as shown Figure 1b. We observed a monotonically decreasing conductivity with FA concentration (Figure S2) and a variety of different JV behaviors depending on the cation composition. In the absence of FA, a fairly ohmic JV relation with relatively little hysteresis between forward and reverse biasing is observed, as expected.[37] In contrast, for samples containing 75% FA, a non-ohmic response was detected in the JV behavior. At bias >0.25 V we see evidence of hysteresis between forward and reverse curves which is not apparent at lower voltages (Figure 1b). In samples containing 15% FA, strongly nonlinear JV behavior as well as large hysteresis before forward and reverse biasing suggests the presence of a reversible resistive switching process. Such dynamic hysteretic behavior presents difficulties for accurate reporting of perform-
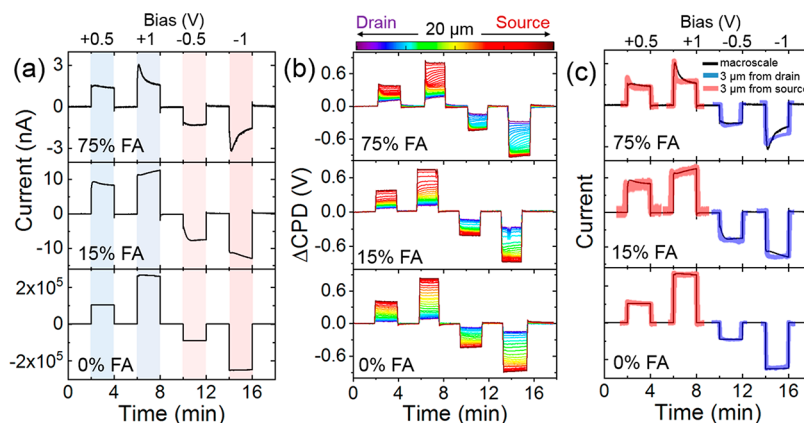
Figure 2. (a) Macroscale current response to voltage pulses at −0.5, −1, +0.5, and +1 V bias. Each voltage pulse was applied for 2 min, with 2 min of 0 V bias between pulses. Top axis shows magnitude of bias and shaded regions show duration of applied bias. Current was measured in-plane with 20 μm electrode spacing. (b) Contact potential difference (ΔCPD) measured using KPFM at different distances from source to drain electrodes during application of the same bias pulse sequence shown in (a). (c) Qualitative comparison of macroscale current response extracted from (a) (black line) with ΔCPD measured 3 μm from drain electrode (blue line) and ΔCPD measured 3 μm from source electrode (red line). Correlation between the local CPD and macroscale current response indicate similar charge dynamics observed at different spatial scales.

ance values in HOIP solar cells.[14] At the same time, if hysteresis can be understood and tuned, then opportunities for HOIP-based memristors[11] and memory devices may be realized.[38,39] Thus, linear *JV* characterization is not well-suited for delineation of complex behaviors, particularly because of the influence of sweep rate, bias polarity, and history effects.[19]

The dielectric frequency response of HOIP films of different compositions was characterized by impedance spectroscopy (IS). From inspection of the Bode (Figure 1c) and Nyquist plots (Figure S3a) it was found that in the absence of FA a single fast charge transport process dominates the dielectric response. In the presence of 15% FA the impedance spectra suggest at least two relaxation processes. For samples containing 75% FA, a slow process begins to dominate at frequencies below ~0.1 Hz. The estimated distribution of the relaxation times (Figure S3b) associated with these processes shows a similar trend. While we see evidence of numerous overlapping processes, incorporation of FA into the perovskite lattice generally suppresses contributions from fast processes on microsecond time scales. The characteristic times for FA = 0%, 15%, and 75% were 9.2 μs, 15.5 ms, and 10 s, respectively.

To complement frequency-dependent measurements, we performed pulsed amperometry experiments to examine the effect of FA charge polarization and relaxation dynamics in the time domain. Transient currents were studied by using a sequence of 2 min voltage pulses which were applied across the HOIP film; each pulse was separated by 2 min of 0 V bias. In the absence of FA, fast (<1 s) current response was observed (Figure 2a, bottom panel). Figure S16 shows dynamic current response on a <1 s time scale. The fast charge relaxation dynamics measured by using pulsed voltammetry were consistent with impedance spectroscopy results, which showed that switching behavior occurred over longer time scales in the presence of FA (Figure S3b).

For HOIP films with 75% FA, polarization/relaxation kinetics is much slower, observed over 2 min for application of ±1 V biases (Figure 2a, top panel). The current response to 500 mV pulse shows a bimodal response with a fast polarization process followed by slower process which stabilize within the 2 min pulse (see Figure S17). A film with 75% FA HOIP shows evidence of a fast polarization followed by a clear

transient relaxation process, while a 15% FA film shows linear temporal response. The diffusion coefficient of a vacancy-assisted migration of iodide was reported to be 3.1×10^{-9} cm²/s ($E_a = 0.3$ eV). For MA ion the diffusion coefficient is 3 orders of magnitude smaller (3.4×10^{-12} cm²/s), and the corresponding activated energy is 3 times higher, $E_a = 0.9$ eV.[40,41] The slowest diffusion is anticipated for the large size of a FA ion. On the basis of this consideration, we assign the slowest process observed for 75% FA HOIP to FA associated ionic subsystem. Overall, the observed sample response in IS and pulsed voltammetry experiments indicates that the charge transport depends on organic cation composition (FA/MA ratio), showing complex (second or mixed-order) relaxation dynamic processes. Results of IS and pulsed amperometry experiments allow us to conclude that exchange of MA with FA in HOIP slows charge polarization/relaxation from ~10s kHz dynamics (microseconds relaxation time) in the absence of FA to sub-Hz (corresponding to ~10 s relaxation time) dynamics in films with 75% FA concentration. 0% FA and 75% FA HOIP do not show hysteretic *JV* behavior whereas in HOIP with 15% FA it was detected, suggesting that *JV* hysteresis and relaxation times have a complex, nonlinear relationship.

Local Transport Properties in HOIPs. We studied local charge dynamics by using tr-KPFM with the same bias pulse sequence as shown in Figure 2a. This mode of tr-KPFM is well-suited for probing slow (seconds−minutes) charge dynamics.[22,42] To ease interpretation of the tr-KPFM results, we plotted data as potential profiles (ΔV) by removing the static offsets from the CPD data (e.g., spatial variations in work function). From Figure 2b, ΔV traces are seen to closely resemble the macroscopic current measurement. In general, both macro and local probe measurements indicate that compositions containing 0% FA involve no slow (i.e., seconds−minutes) charge dynamics, whereas films containing 75% FA demonstrate clear relaxation on the scale of minutes. The similarity between macroscale current relaxation behavior and nanoscale potential dynamics indicates correlation between macroscale HOPI film performance and local charge dynamics measured by KPFM. In Figures S4 and S5 we evaluate correlations between macro- and nanoscale relaxation dynamics. Our results indicate that the slow macro relaxation
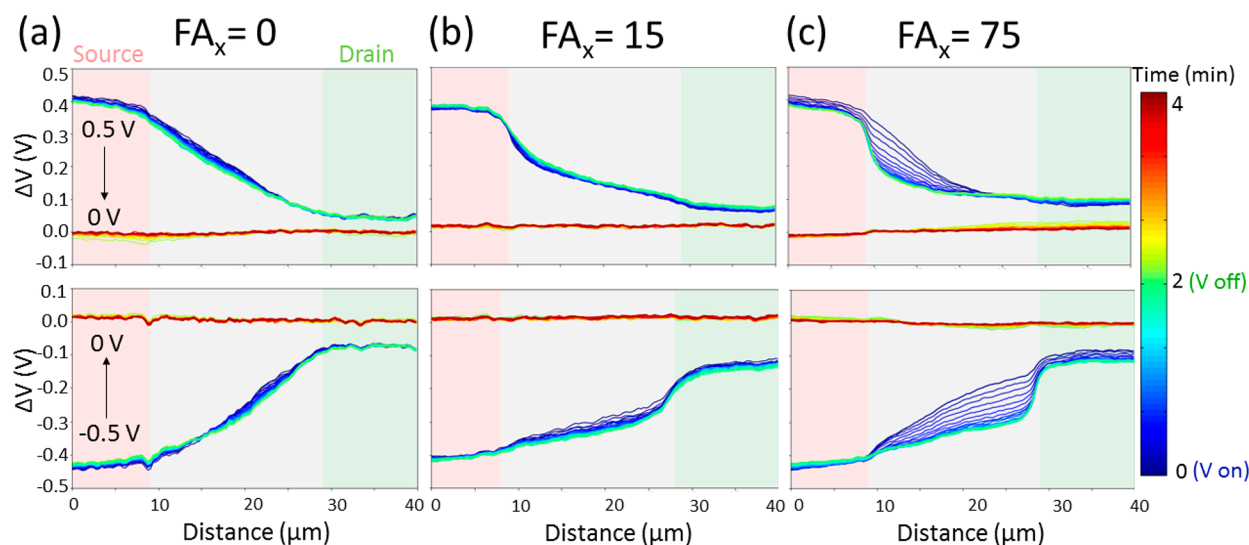
Figure 3. Time-resolved KPFM potentiometry showing the evolution of the potential profile for (a) 0% FA, (b) 15% FA concentrations, and (c) 75% FA concentrations. Temporal evolution of the potential profile is shown for +500 mV (top row) and −500 mV (bottom row) bias applied to the HOIP film. Color scale represents the measurement time (total = 4 min).
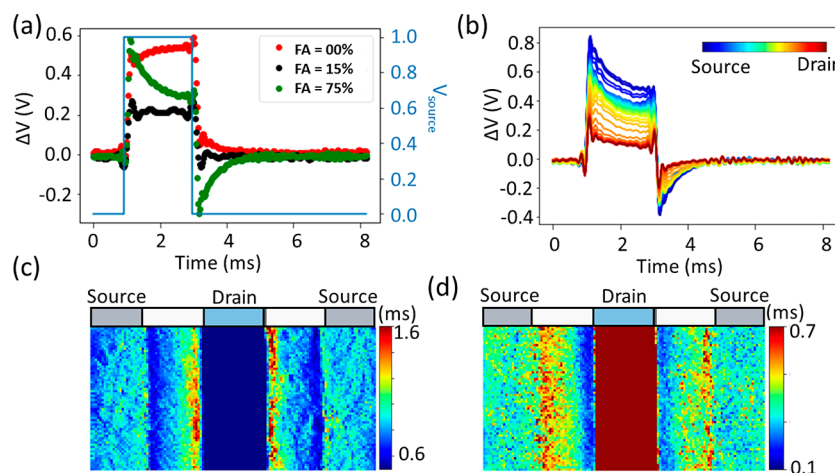

Figure 4. (a) Time spectroscopy voltammetry curves averaged between the source−drain electrode in the areas indicated (white box) in Figure S9. (b) Spatial variability in the relaxation between source and drain electrode for 75% FA. (c) Relaxation maps determined from exponential fitting of the G-KPFM data for 75% FA during pulsing with (c) 1 V and (d) −1 V (bias on) and discharging (bias off) potential distribution are shown in the top and bottom rows consecutively. Image size is 40 × 80 μm^2.

with a time constant of ∼30 s correlates with the nanoscale response ($\tau \sim 26 \pm 2$ s) observed at a distance of <5 μm from the anode for either forward (+1 V) or reverse (−1 V) biasing of the HOIP film. This result implies that for 75% FA the bulk HOIP film behavior is governed by slow, ionically mediated charge transport mechanisms detected by tr-KPFM. The small transient observed for 0% FA HOIP (Figure S6) indicates that tr-KPFM can detect local phenomena which may not contribute to macroscale response.

In Figure 3, the potential profiles between the source−HOIP−drain are plotted as a function of time during and after the application of 500 mV across electrodes. The temporal evolution of the corresponding electric fields is shown in Figure S7 approximated from ΔV profiles as $E(x) = -\frac{d}{dx}\Delta V(x)$, where x is the position across the HOIP film profile. In Table S2 we summarize the main findings from the slow tr- KPFM measurements for the samples tested under

forward and reverse biasing conditions, including the presence of interfacial effects.

For both 0% and 15% FA films, we observe a slight temporal drift in the and small kinks in the potential profile close to the negative electrode in the case of 0% FA. Birkhold et al. assigned these features to the reduction of Pb^{2+} to Pb^0 at the Au electrode was responsible for this slow drift and kinks at the cathode interface.[22] While we are operating at much lower voltages, using inert Pt electrodes, we do not expect charge injection to play as significant of a role; however, we do not fully rule out the impact of charge injection and or surface conductivity effects.

From Figure 3a, we observe for the 0% FA HOIP a linear potential drop (constant electric field) between the electrodes and little or no evidence of any interface polarization at either perovskite−electrode interface. This is consistent with the ohmic nonhysteretic behavior observed in JV measurements. For the 15% FA HOIP film we see an ∼150 mV potential drop at the anode, with a <∼40 mV potential at the cathode. For

75% FA HOIP film we observe a drift in the potential over time until compact <5 μm space charge region is established at the anodic interface, corresponding to a potential drop of ~290 mV. We conclude that the slow screening is predominately related to ionic space charge regions arising from a buildup of negative charge at the anode, and it is proportional to FA loading. However, tr-KPFM does not enable identification of the ionic species that are accumulated at the anode.

We investigated charge dynamics on microseconds–milliseconds time scales using time-resolved G-KPFM (temporal resolution of ~10 μs) with HOIP films excited with ~2 ms pulses to avoid DC contributions.[43,44] Figure 4a summarizes the data as time-resolved potentiometry spectra, averaged over the channel regions indicated in Figure S8. It is evident that on the microseconds–milliseconds time scales the most pronounced charge transients occur in 75% FA HOIP film, which correlate with slow processes observed in macroscale measurements and in tr-KPFM (Figure 2). Upon −1 V pulse excitation, we observe relaxation with fast and slow components for 0 and 75% FA HOIP samples (Figure S8). The fast (hundreds of microseconds) component for 0% FA HOIP which was measured by tr-KPFM suggests the presence of additional fast screening mechanisms which were not immediately clear from the macroscale measurements alone. The time scale of these events would still suggest that they are associated with ionic mechanisms. However, clearly the time scales are much slower than that measured in Figure 2c. From the perspective of bulk diffusion, its has been demonstrated that migration of I$^-$ is several orders of magnitude faster than MA$^+$ ions (milliseconds vs seconds);[45] however, it is difficult to assign this precisely or to fully rule out other factors such as transport of mobile surface ions.

Figure 4b displays spatiotemporal variability of voltage drop between the electrodes for 75% FA (data for 0% and 15% FA loadings are provided in Figure S13). Comparing these plots confirms that at these time scales 0 and 75% FA involve charge redistribution, whereas 15% rapidly responds to the applied bias without subsequent charge relaxation. Based on the results so far, the presence of charge dynamics in the case of 0% FA and absence in 15% may come as a surprise. It also indicates that there are similarities in behaviors of both 0% and 75% FA, at least at fast time scales.

Spatial maps of the CPD averaged over time for polarizing (~2 ms) and depolarizing (~2 ms) events are shown in Figures S9 and S10 for +1 and −1 V biases, respectively. To visualize the fast polarization dynamics, Figures S11 and S12 show plots of the time-resolved potential profiles, electric field, and charge density across the gap (like Figure 3).

Comparing the time-averaged potential during "on" and "off" polarization states for +1 and −1 V (Figures S9 and S10, respectively), a striking contrast is seen for 15% FA loading. During the relaxation after +1 V, we observe a compact (<1 μm) space charge region close to the anode, corresponding to a more negatively doped region (Figure S9). After application of −1 V, we observe no space charge region formation (Figure S10). Furthermore, charge screening for 15% FA HOIP (also largest hysteresis) is an instantaneous, polarity-independent process which is confined to the source electrode. For 0% or 75% FA HOIP films (smallest hysteresis) we observe dynamic screening, with the charge buildup at anode and cathode interfaces and a redistribution of charge between the electrodes during the 2 ms measurement window.

The presence of interfacial dipole charge has previously been reported in mixed FA/MA HOIP cross sections.[23] Using the lower temporal resolution (~milliseconds) tr-KPFM method, Weber et al. reported a negative space charge buildup in the perovskite interface within ~3 ms after switching on an electric field, which relaxes over ~120 ms through the migration of positive charges. They concluded that formation and release of trapped ionic charges at the interfaces was a dominant mechanism of hysteresis, whereas bulk diffusion of ions appears as slow relaxation component.[23] They speculated that stabilization of the negative charge at the cathode interface was a result of chemical binding or complexation of ions at the interfaces. We note that in our case time scale of the interface screening for the 15% FA HOIP is much faster than our current measurement resolution (<microseconds), suggesting that either electronic/atomic or dipole reorientation is the more likely mechanism for the observed interface dipole.

It is important to compare fast and slow relaxation dynamics on nanoscale and macroscale extracted from IS. We summarized the results of the G-KPFM measurements in Table S3. Evidence of intermediate/slow response from IS experiment for the 15% FA sample indicates slow (~10 ms) charge registration. For 0% and 75% FA loadings, for forward bias the large potential drop at the cathode, which is suppressed at longer time scales, can be understood by considering a coupled electronic–ionic screening mechanism in which there is a delayed buildup of the anion concentration at the anode (correlated to the depletion of its concentration at the cathode) under the built-in electronic field.

Figure 4c,d shows calculated relaxation time constants for 75% FA HOIP sample excited with +1 and −1 V pulses, estimated from fitting the time-dependent response to exponential decay. For +1 V (Figure 4c), the relaxation is faster at the source electrode interface, while considerably slower relaxation is observed near the drain electrode. For −1 V bias pulse (Figure S8), relaxation is faster at the drain electrode interface, and considerably slower relaxation is observed near the source electrode. This result suggests that in the 75% FA case we observe charge transport at both fast (hundreds of microseconds) and slow (tens of seconds) time scales. In addition, we found that at the microseconds–milliseconds time scale that relaxations were similar in 0% and 75% FA HOIP samples, strongly suggesting a similar screening mechanism. In comparison, for 15% FA loading, we observe little or no relaxation processes within the measurement window. Altogether, these results indicate that the observed space charge regions (Figure S9b) for 15% FA HOIP involve faster charge transport processes (e.g., electronic conduction, dipolar reorientation) than is accessible by G-KPFM measurement (~10 μs resolution). The observation of fast screening for 0% and 75% FA HOIP suggests that both samples involve intrinsic electronic–ionic coupling mechanisms. Our results indicate that it is likely that observed hysteresis in HOIP can have disparate underlying mechanisms.

To rationalize experimental results in the context of FA effects on MAPbI$_3$ lattice dynamics, we performed AIMD at 300 K (see the Experimental Methods section). We consider parent perovskites, MAPbI$_3$, as well as its mixed cation counterparts, MA$_x$FA$_{1-x}$PbI$_3$ (x = 0.875, 0.25), to closely model the experimental lattices. Note that here fractions of cations are defined by the stoichiometric ratio for the calculated periodic unit cell. First, the dynamics of the PbI framework are analyzed through the calculated respective root-

mean-square fluctuations (RMSF) shown in Figure S13a and Table S4. Larger RMSF indicates increased structural fluctuations in lattices involving increased FA loading. Note that, as expected, the heavier Pb atoms fluctuate less than the lighter I atoms in all the hybrid perovskite systems considered (left corner of Figure S13a). Furthermore, we find that the radial distribution function of Pb−I becomes broader with FA loading, again indicating greater lattice dynamics in these mixed cation perovskites (see Figure S14a,b). Besides the inorganic framework, we also investigate the effect of cation mixing on the dynamical properties of MA inside the cuboctahedral PbI framework. Figure S13b shows much faster decay in the autocorrelation function for MA in the 75% FA case compared to the parent MAPbI$_3$ material. The faster rotation of MA further weakens the hydrogen bonding between MA and PbI as shown in Figure S15. Thus, with FA loading, rotational degrees of freedom become more pronounced for MA inside the PbI framework. This is attributed to the fact that the size of FA cations is larger than that of MA ones, and FA loading leads to a strain and a staggered lattice. Subsequently, the lattice constant is becoming larger, increasing rotational freedom of MA cations. Overall, the enhanced lattice fluctuations can directly affect the ion migration in these halide perovskites under ambient operating conditions. It is widely accepted that fast ion migration in these materials occurs through hopping of ions to the nearest point-defect site.[17,46] During this defect-mediated hopping, the local structure gets distorted and eventually gives rise to an activation energy for the ion migration process. When the lattice is dynamically flexible, the local distortion is much less prominent, and that consequently results in decrease in the activation energy for ion migration. In this study, we find that FA loading enhances the structural fluctuations in MA$_x$FA$_{1-x}$PbI$_3$, making the lattice more flexible toward any local distortions. This, in turn, helps the migrating ions to move faster by sequential hopping process. This is consistent with the previous reports showing the effect of dynamical flexible lattices for charge and ion migration in halide perovskites.[47]

CONCLUSIONS

In summary, we demonstrated an experimental approach to correlate transport behavior and relaxation processes in thin films on macro- and nanoscales through a combination of time- and frequency-dependent measurements in combination with electronic structure modeling. Frequency-dependent measurements probe dynamics of the charge transfer process on the microseconds−seconds time scales, enabling investigation of the nature of FA effects on ion dynamics as corroborated by modeling insights into the enhanced lattice fluctuations with FA loading. We observe that increased FA loading leads to slowing of processes from microseconds to second time scales. The time-dependent pulsed techniques (macro- and nanoscale) allow for insights into film polarization relaxation dynamics including both global (across the entire sample) and local imaging. We finally show the heterogeneous nature of the relaxation times, which can be related to local structural/compositional peculiarities as well as accumulation of FA at the electrode surface and relative distance from the electrode. These experimental observations paint a consistent picture of physical processes emerging in complex hybrid perovskite materials with modification of structural composition across multiple time and length scales, demonstrating the utility of using multiple complementary techniques and serving as a guideline for future development of high-performance devices.

EXPERIMENTAL METHODS

Material Synthesis. The HOIP was grown on an insulating SiO$_2$ substrate with prepatterned interdigitated platinum electrodes with 20 μm separation. We employed an in-plane device configuration to enable probing of the HOIP layer without considering the impact of the charge transport layers and to allow direct measurement of the potential and electric field distribution between electrodes. The mixed cation perovskite precursor was made by mixing cesium iodide, methylammonium iodide (MAI), formamidine iodide (FAI), methylammonium chloride (MACl), and lead iodide (PbI$_2$) at molar ratio of 0.05:66x:6y:0.25:1 in dimethyl sulfoxide. To change the molar ratio of MA and FA, we vary x for MAI from 0 to 0.75 and y for FAI from 0 to 0.7. 5% of Cs was used to stabilize the structure. Note 25% of MACl was employed to maintain the film quality, and this kept the MA concentration in the range of 25%−100%. The thin film is deposited by the "hot-casting" approach; briefly, the substrates were preheated at 170 °C and quickly transferred to spin-coater chunk. The precursor was preheated at 100 °C and was quickly dropped on the substrate, and the spin coating started within 10 s and reaches 4000 rpm without ramping.

Broadband Macroscopic Methods. Electrical impedance was measured by using a Zahner IM6 electrochemical workstation with 50 mVAC excitation and 0 V DC offset from 100 mHz to 1 MHz. Current−voltage (JV) characteristics were measured by using a Keithley 2420 source-measure unit in forward and reverse directions from 0 to ±1 V with a sweep rate of 20 mV/s. For pulsed voltammetry measurements, pulses were applied sequentially for 2 min each with −0.5, −1, +0.5, and +1 V biases. All JV and pulsed measurements were performed by using custom LabVIEW software. All measurements were performed in the dark in air. The impedance data were tested for linearity, causality, and stability by using Kramers−Kronig (KK) transformations showing good agreement, with <3% deviation at the low-frequency part of the impedance trace. The KK fit was further used for DTR modeling. The estimated distribution of relaxation times (Figure S1e) was calculated by using the DTRTOOLS Matlab toolbox.

Local KPFM Measurements. All nanoscale measurements were performed by using a Cypher AFM system (Asylum Research, an Oxford Instruments company) and a conductive Pt/Ir-coated cantilever (PPP-EFM Nanosensors). KPFM measurements were performed in lift mode or dual pass mode at a height of 50 nm unless stated otherwise. Very briefly, the first pass was performed in tapping mode for measuring surface height, and during the second pass the tip traced the topography profile with an additional height offset used for measuring the KPFM surface potential. The measured KPFM CPD was processed to remove intrinsic work function differences between tip and sample. This was achieved by subtracted the profile of the grounded device ($V_{device} = 0$) from the profiles obtained during operandi conditions ($V_{device} > 0$), leading to a local measure of the device potential ($\Delta V = CPD(V_{device}) − CPD(0)$). The G-Mode was performed by using a LabVIEW/Matlab controller implemented in PXI architecture using National Instruments NI-6124 fast AWG and DAQ cards. A description of the technical realization of G-KPFM was provided previously.[43] Briefly, at each spatial location we capture contact potential difference (CPD) during a charging (bias on) and discharging (bias off) event. In this way, each voltage pulse simulates a forward (0−1 V) and reverse (1−0 V) voltage. The resultant G-Mode KPFM data set is a 3-dimensional CPD (x, y, time) data set where each spatial point contains a measure of any potential relaxation behavior (if present) under the AFM tip.

MD Simulations. Well-established and tested AIMD techniques were applied in this study.[48,49] The parent MAPbI$_3$ was modeled by a large 4 × 2 × 2 supercell (containing 768 atoms), enabling us to resolve FA loading concentration up to 12.5% and to provide a good statistical sample size for the exploring structural dynamics. Various

compositions which are very close to our experimental study were considered by substituting FA for MA. For each composition, various ordered and disordered configurations of the A-site species were considered, and the lowest energy structure was selected for dynamics. We have done AIMD simulations at a temperature of 300 K using the CP2K code.[49] The QUICKSTEP formalism was applied where the mixed Gaussian and plane-wave method has been used. We employed GGA of the PBEsol form, analytical dual-space pseudopotentials, and Grimme-type (DFT-D3) dispersion corrections.[50−52] Each simulation covered a simulation time period of 20 ps with a time step of 1 fs. These systems take 3−4 ps to reach equilibrium, and so we used the rest of the time for analysis. Equilibrium dynamics were simulated in the NPT ensemble using a Nosé−Hoover thermostat and a barostat as formulated by Martyna et al.[53]

■ ASSOCIATED CONTENT

ⓈⒾ Supporting Information

The Supporting Information is available free of charge at https://pubs.acs.org/doi/10.1021/acsami.0c00561.

> Review of experimental characterization tools to study macro- and micro/nanoscale charge transport, current at 1 V from *IV* curves, Nyquist plots, KPFM, G-KPFM results, spatial variability of relaxation time, lattice and cation dynamics in $MA_xFA_{1−x}PbI_3$ (PDF)

■ AUTHOR INFORMATION

Corresponding Authors

Liam Collins − *Center for Nanophase Materials Sciences, Oak Ridge National Laboratory, Oak Ridge, Tennessee 37831, United States*; Email: collinslf@ornl.gov

Ilia N. Ivanov − *Center for Nanophase Materials Sciences, Oak Ridge National Laboratory, Oak Ridge, Tennessee 37831, United States*; ⓞ orcid.org/0000-0002-6726-2502; Email: ivanovin@ornl.gov

Authors

Eric S. Muckley − *Center for Nanophase Materials Sciences, Oak Ridge National Laboratory, Oak Ridge, Tennessee 37831, United States*; ⓞ orcid.org/0000-0001-7114-5424

Hsinhan Tsai − *Materials Physics and Application Division, Los Alamos National Laboratory, Los Alamos, New Mexico 87545, United States*

Dibyajyoti Ghosh − *Materials Physics and Application Division, Los Alamos National Laboratory, Los Alamos, New Mexico 87545, United States*; ⓞ orcid.org/0000-0002-3640-7537

Amanda J. Neukirch − *Materials Physics and Application Division, Los Alamos National Laboratory, Los Alamos, New Mexico 87545, United States*; ⓞ orcid.org/0000-0002-6583-0086

Sergei Tretiak − *Materials Physics and Application Division, Los Alamos National Laboratory, Los Alamos, New Mexico 87545, United States*; ⓞ orcid.org/0000-0001-5547-3647

Sergei V. Kalinin − *Center for Nanophase Materials Sciences, Oak Ridge National Laboratory, Oak Ridge, Tennessee 37831, United States*; ⓞ orcid.org/0000-0001-5354-6152

Wanyi Nie − *Materials Physics and Application Division, Los Alamos National Laboratory, Los Alamos, New Mexico 87545, United States*

Complete contact information is available at:
https://pubs.acs.org/10.1021/acsami.0c00561

Author Contributions

L.C. and I.I. conceived of the experimental plan. E.M. and I.I. performed acquisition and analysis of the macroscopic measurements. L.C. performed acquisition and analysis of the scanning probe measurements. H.T. and W.N. provided the HOIP samples. D.G., A.J.N., and S.T. performed the MD simulations. L.C., I.I., W.N., and S.T. participated in the discussion and interpretation of results. All authors contributed to the writing of the manuscript.

Notes

The authors declare no competing financial interest.

■ REFERENCES

(1) Kojima, A.; Teshima, K.; Shirai, Y.; Miyasaka, T. Organometal Halide Perovskites as Visible-Light Sensitizers for Photovoltaic Cells. *J. Am. Chem. Soc.* **2009**, *131* (17), 6050−6051.

(2) Lee, M. M.; Teuscher, J.; Miyasaka, T.; Murakami, T. N.; Snaith, H. J. Efficient Hybrid Solar Cells Based on Meso-Superstructured Organometal Halide Perovskites. *Science* **2012**, *338* (6107), 643−647.

(3) Kim, H. S.; Lee, C. R.; Im, J. H.; Lee, K. B.; Moehl, T.; Marchioro, A.; Moon, S. J.; Humphry-Baker, R.; Yum, J. H.; Moser, J. E.; Gratzel, M.; Park, N. G. Lead Iodide Perovskite Sensitized All-Solid-State Submicron Thin Film Mesoscopic Solar Cell With Efficiency Exceeding 9%. *Sci. Rep.* **2012**, *2*, 591.

(4) Juarez-Perez, E. J.; Sanchez, R. S.; Badia, L.; Garcia-Belmonte, G.; Kang, Y. S.; Mora-Sero, I.; Bisquert, J. Photoinduced Giant Dielectric Constant in Lead Halide Perovskite Solar Cells. *J. Phys. Chem. Lett.* **2014**, *5* (13), 2390−2394.

(5) Dualeh, A.; Moehl, T.; Tetreault, N.; Teuscher, J.; Gao, P.; Nazeeruddin, M. K.; Gratzel, M. Impedance Spectroscopic Analysis of Lead Iodide Perovskite-Sensitized Solid-States Solar Cells. *ACS Nano* **2014**, *8* (1), 362−373.

(6) Snaith, H. J.; Abate, A.; Ball, J. M.; Eperon, G. E.; Leijtens, T.; Noel, N. K.; Stranks, S. D.; Wang, J. T.; Wojciechowski, K.; Zhang, W. Anomalous Hysteresis in Perovskite Solar Cells. *J. Phys. Chem. Lett.* **2014**, *5* (9), 1511−1515.

(7) Calado, P.; Telford, A. M.; Bryant, D.; Li, X.; Nelson, J.; O'Regan, B. C.; Barnes, P. R. Evidence for Ion Migration in Hybrid Perovskite Solar Cells with Minimal Hysteresis. *Nat. Commun.* **2016**, *7*, 13831.

(8) Chen, B.; Yang, M.; Priya, S.; Zhu, K. Origin of J-V Hysteresis in Perovskite Solar Cells. *J. Phys. Chem. Lett.* **2016**, 7 (5), 905−917.

(9) Cojocaru, L.; Uchida, S.; Tamaki, K.; Jayaweera, P. V.; Kaneko, S.; Nakazaki, J.; Kubo, T.; Segawa, H. Determination of Unique Power Conversion Efficiency of Solar Cell Showing Hysteresis in the IV Curve Under Various Light Intensities. *Sci. Rep.* **2017**, 7 (1), 11790.

(10) Nemnes, G. A.; Besleaga, C.; Stancu, V.; Dogaru, D. E.; Leonat, L. N.; Pintilie, L.; Torfason, K.; Ilkov, M.; Manolescu, A.; Pintilie, I. Normal and Inverted Hysteresis in Perovskite Solar Cells. *J. Phys. Chem. C* **2017**, 121 (21), 11207−11214.

(11) Tress, W. Metal Halide Perovskites as Mixed Electronic-Ionic Conductors: Challenges and Opportunities-From Hysteresis to Memristivity. *J. Phys. Chem. Lett.* **2017**, 8 (13), 3106−3114.

(12) Unger, E. L.; Hoke, E. T.; Bailie, C. D.; Nguyen, W. H.; Bowring, A. R.; Heumuller, T.; Christoforo, M. G.; McGehee, M. D. Hysteresis and Tansient Behavior in Current-Voltage Measurements of Hybrid-Perovskite Absorber Solar Cells. *Energy Environ. Sci.* **2014**, 7 (11), 3690−3698.

(13) Weber, S. A. L.; Hermes, I. M.; Turren-Cruz, S. H.; Gort, C.; Bergmann, V. W.; Gilson, L.; Hagfeldt, A.; Graetzel, M.; Tress, W.; Berger, R. How the Formation of Interfacial Charge Causes Hysteresis in Perovskite Solar Cells. *Energy Environ. Sci.* **2018**, 11 (9), 2404−2413.

(14) Nemnes, G. A.; Besleaga, C.; Tomulescu, A. G.; Palici, A.; Pintilie, L.; Manolescu, A.; Pintilie, I. How Measurement Protocols Influence the Dynamic JV Characteristics of Perovskite Solar cells: Theory and Experiment. *Sol. Energy* **2018**, 173, 976−983.

(15) Conings, B.; Drijkoningen, J.; Gauquelin, N.; Babayigit, A.; D'Haen, J.; D'Olieslaeger, L.; Ethirajan, A.; Verbeeck, J.; Manca, J.; Mosconi, E.; De Angelis, F.; Boyen, H. G. Intrinsic Thermal Instability of Methylammonium Lead Trihalide Perovskite. *Adv. Energy Mater.* **2015**, 5 (15), 1500477.

(16) Wang, D.; Wright, M.; Elumalai, N. K.; Uddin, A. Stability of Perovskite Solar Cells. *Sol. Energy Mater. Sol. Cells* **2016**, 147, 255−275.

(17) Yuan, Y.; Huang, J. Ion Migration in Organometal Trihalide Perovskite and Its Impact on Photovoltaic Efficiency and Stability. *Acc. Chem. Res.* **2016**, 49 (2), 286−293.

(18) Park, N. G.; Gratzel, M.; Miyasaka, T.; Zhu, K.; Emery, K. Towards Stable and Commercially Available Perovskite Solar Cells. *Nat. Energy* **2016**, 1 (11), 16152.

(19) Christians, J. A.; Manser, J. S.; Kamat, P. V. Best Practices in Perovskite Solar Cell Efficiency Measurements. Avoiding the Error of Making Bad Cells Look Good. *J. Phys. Chem. Lett.* **2015**, 6 (5), 852−857.

(20) Guerrero, A.; You, J.; Aranda, C.; Kang, Y. S.; Garcia-Belmonte, G.; Zhou, H.; Bisquert, J.; Yang, Y. Interfacial Degradation of Planar Lead Halide Perovskite Solar Cells. *ACS Nano* **2016**, 10 (1), 218−224.

(21) Roiati, V.; Mosconi, E.; Listorti, A.; Colella, S.; Gigli, G.; De Angelis, F. Stark Effect in Perovskite/TiO$_2$ Solar Cells: Evidence of Local Interfacial Order. *Nano Lett.* **2014**, 14 (4), 2168−2174.

(22) Birkhold, S. T.; Precht, J. T.; Liu, H. B.; Giridharagopal, R.; Eperon, G. E.; Schmidt-Mende, L.; Li, X. S.; Ginger, D. S. Interplay of Mobile Ions and Injected Carriers Creates Recombination Centers in Metal Halide Perovskites under Bias. *Acs Energy Lett.* **2018**, 3 (6), 1279−1286.

(23) Hermes, I. M.; Hou, Y.; Bergmann, V. W.; Brabec, C. J.; Weber, S. A. L. The Interplay of Contact Layers: How the Electron Transport Layer Influences Interfacial Recombination and Hole Extraction in Perovskite Solar Cells. *J. Phys. Chem. Lett.* **2018**, 9 (21), 6249−6256.

(24) Haruyama, J.; Sodeyama, K.; Han, L.; Tateyama, Y. First-Principles Study of Ion Diffusion in Perovskite Solar Cell Sensitizers. *J. Am. Chem. Soc.* **2015**, 137 (32), 10048−10051.

(25) Bakulin, A. A.; Selig, O.; Bakker, H. J.; Rezus, Y. L.; Muller, C.; Glaser, T.; Lovrincic, R.; Sun, Z.; Chen, Z.; Walsh, A.; Frost, J. M.; Jansen, T. L. Real-Time Observation of Organic Cation Reorientation in Methylammonium Lead Iodide Perovskites. *J. Phys. Chem. Lett.* **2015**, 6 (18), 3663−3669.

(26) Leguy, A. M.; Goni, A. R.; Frost, J. M.; Skelton, J.; Brivio, F.; Rodriguez-Martinez, X.; Weber, O. J.; Pallipurath, A.; Alonso, M. I.; Campoy-Quiles, M.; Weller, M. T.; Nelson, J.; Walsh, A.; Barnes, P. R. Dynamic Disorder, Phonon Lifetimes, and the Assignment of Modes to the Vibrational Spectra of Methylammonium Lead Halide Perovskites. *Phys. Chem. Chem. Phys.* **2016**, 18 (39), 27051−27066.

(27) Leguy, A. M. A.; Frost, J. M.; McMahon, A. P.; Sakai, V. G.; Kockelmann, W.; Law, C.; Li, X.; Foglia, F.; Walsh, A.; O'Regan, B. C.; Nelson, J.; Cabral, J. T.; Barnes, P. R. F. The Dynamics of Methylammonium Ions in Hybrid Organic-Inorganic Perovskite Solar Cells. *Nat. Commun.* **2015**, 6, 7124.

(28) Lee, J. H.; Bristowe, N. C.; Lee, J. H.; Lee, S. H.; Bristowe, P. D.; Cheetham, A. K.; Jang, H. M. Resolving the Physical Origin of Octahedral Tilting in Halide Perovskites. *Chem. Mater.* **2016**, 28 (12), 4259−4266.

(29) Yang, B.; Brown, C. C.; Huang, J. S.; Collins, L.; Sang, X. H.; Unocic, R. R.; Jesse, S.; Kalinin, S. V.; Belianinov, A.; Jakowski, J.; Geohegan, D. B.; Sumpter, B. G.; Xiao, K.; Ovchinnikova, O. S. Enhancing Ion Migration in Grain Boundaries of Hybrid Organic-Inorganic Perovskites by Chlorine. *Adv. Funct. Mater.* **2017**, 27 (26), 1700749.

(30) Zolfaghari, Z.; Hassanabadi, E.; Pitarch-Tena, D.; Yoon, S. J.; Shariatinia, Z.; van de Lagemaat, J.; Luther, J. M.; Mora-Seró, I. Operation Mechanism of Perovskite Quantum Dot Solar Cells Probed by Impedance Spectroscopy. *Acs Energy Lett.* **2019**, 4 (1), 251−258.

(31) Pitarch-Tena, D.; Ngo, T. T.; Vallés-Pelarda, M.; Pauporté, T.; Mora-Seró, I. Impedance Spectroscopy Measurements in Perovskite Solar Cells: Device Stability and Noise Reduction. *Acs Energy Lett.* **2018**, 3 (4), 1044−1048.

(32) Wang, P.; Ulfa, M.; Pauporté, T. Effects of Perovskite Monovalent Cation Composition on the High and Low Frequency Impedance Response of Efficient Solar Cells. *J. Phys. Chem. C* **2018**, 122 (4), 1973−1981.

(33) Guerrero, A.; Garcia-Belmonte, G.; Mora-Sero, I.; Bisquert, J.; Kang, Y. S.; Jacobsson, T. J.; Correa-Baena, J. P.; Hagfeldt, A. Properties of Contact and Bulk Impedances in Hybrid Lead Halide Perovskite Solar Cells Including Inductive Loop Elements. *J. Phys. Chem. C* **2016**, 120 (15), 8023−8032.

(34) Song, T. B.; Yuan, Z. H.; Mori, M.; Motiwala, F.; Segev, G.; Masquelier, E.; Stan, C. V.; Slack, J. L.; Tamura, N.; Sutter-Fella, C. M. Revealing the Dynamics of Hybrid Metal Halide Perovskite Formation via Multimodal In Situ Probes. *Adv. Funct. Mater.* **2020**, 30, 1908337.

(35) Collins, L.; Kilpatrick, J. I.; Kalinin, S. V.; Rodriguez, B. J. Towards Nanoscale Electrical Measurements in Liquid by Advanced KPFM Techniques: a Review. *Rep. Prog. Phys.* **2018**, 81 (8), 086101.

(36) Sadewasser, S.; Nicoara, N. Time-Resolved Electrostatic and Kelvin Probe Force Microscopy. In *Kelvin Probe Force Microscopy*; Springer: 2018; pp 119−143.

(37) Nie, W.; Tsai, H.; Asadpour, R.; Blancon, J. C.; Neukirch, A. J.; Gupta, G.; Crochet, J. J.; Chhowalla, M.; Tretiak, S.; Alam, M. A.; Wang, H. L.; Mohite, A. D. Solar Cells. High-efficiency Solution-Processed Perovskite Solar Cells with Millimeter-Scale Grains. *Science* **2015**, 347 (6221), 522−525.

(38) Gu, C.; Lee, J. S. Flexible Hybrid Organic-Inorganic Perovskite Memory. *ACS Nano* **2016**, 10 (5), 5413−8.

(39) Zhu, X.; Lee, J.; Lu, W. D. Iodine Vacancy Redistribution in Organic-Inorganic Halide Perovskite Films and Resistive Switching Effects. *Adv. Mater.* **2017**, 29 (29), 1700527.

(40) Futscher, M. H.; Lee, J. M.; McGovern, L.; Muscarella, L. A.; Wang, T.; Haider, M. I.; Fakharuddin, A.; Schmidt-Mende, L.; Ehrler, B. Quantification of ion migration in CH$_3$NH$_3$PbI$_3$ perovskite solar cells by transient capacitance measurements. *Mater. Horiz.* **2019**, 6 (7), 1497−1503.

(41) Eames, C.; Frost, J. M.; Barnes, P. R. F.; O'Regan, B. C.; Walsh, A.; Islam, M. S. Ionic transport in hybrid lead iodide perovskite solar cells. *Nat. Commun.* **2015**, 6 (1), 7497.

(42) Strelcov, E.; Ahmadi, M.; Kalinin, S. V. Nanoscale Transport Imaging of Active Lateral Devices: Static and Frequency Dependent Modes. In *Kelvin Probe Force Microscopy*; Springer: 2018; pp 251−329.

(43) Collins, L.; Ahmadi, M.; Wu, T.; Hu, B.; Kalinin, S. V.; Jesse, S. Breaking the Time Barrier in Kelvin Probe Force Microscopy: Fast Free Force Reconstruction Using the G-Mode Platform. *ACS Nano* **2017**, *11* (9), 8717−8729.

(44) Collins, L.; Belianinov, A.; Somnath, S.; Balke, N.; Kalinin, S. V.; Jesse, S. Full Data Dcquisition in Kelvin Probe Force Microscopy: Mapping Dynamic Electric Phenomena in Real Space. *Sci. Rep.* **2016**, *6*, 30557.

(45) Futscher, M. H.; Lee, J. M.; McGovern, L.; Muscarella, L. A.; Wang, T.; Haider, M. I.; Fakharuddin, A.; Schmidt-Mende, L.; Ehrler, B. Quantification of ion migration in CH 3 NH 3 PbI 3 perovskite solar cells by transient capacitance measurements. *Mater. Horiz.* **2019**, *6* (7), 1497−1503.

(46) Eames, C.; Frost, J. M.; Barnes, P. R.; O'Regan, B. C.; Walsh, A.; Islam, M. S. Ionic Transport in Hybrid Lead Iodide Perovskite Solar Cells. *Nat. Commun.* **2015**, *6*, 7497.

(47) Tsai, H.; Asadpour, R.; Blancon, J. C.; Stoumpos, C. C.; Durand, O.; Strzalka, J. W.; Chen, B.; Verduzco, R.; Ajayan, P. M.; Tretiak, S.; Even, J.; Alam, M. A.; Kanatzidis, M. G.; Nie, W.; Mohite, A. D. Light-Induced Lattice Expansion Leads to High-efficiency Perovskite Solar Cells. *Science* **2018**, *360* (6384), 67−70.

(48) Hutter, J.; Iannuzzi, M.; Schiffmann, F.; VandeVondele, J. cp2k: ATomistic Simulations of Condensed Matter systems. *WIREs Comput. Mol. Sci.* **2014**, *4*, 15−25.

(49) VandeVondele, J.; Krack, M.; Mohamed, F.; Parrinello, M.; Chassaing, T.; Hutter, J. QUICKSTEP: Fast and Accurate Density Functional Calculations Using a Mixed Gaussian and Plane Waves Approach. *Comput. Phys. Commun.* **2005**, *167* (2), 103−128.

(50) Perdew, J. P.; Ruzsinszky, A.; Csonka, G. I.; Vydrov, O. A.; Scuseria, G. E.; Constantin, L. A.; Zhou, X.; Burke, K. Restoring the Density-Gradient Expansion for Exchange in Solids and Surfaces. *Phys. Rev. Lett.* **2008**, *100* (13), 136406-1−136406-4.

(51) Goedecker, S.; Teter, M.; Hutter, J. Separable Dual-space Gaussian Pseudopotentials. *Phys. Rev. B: Condens. Matter Mater. Phys.* **1996**, *54* (3), 1703−1710.

(52) Grimme, S.; Antony, J.; Ehrlich, S.; Krieg, H. A Consistent and Accurate ab initio Parametrization of Density Functional Dispersion Correction (DFT-D) for the 94 elements H-Pu. *J. Chem. Phys.* **2010**, *132* (15), 154104-1−154104-18.

(53) Martyna, G. J.; Tobias, D. J.; Klein, M. L. Constant-Pressure Molecular-Dynamics Algorithms. *J. Chem. Phys.* **1994**, *101* (5), 4177−4189.